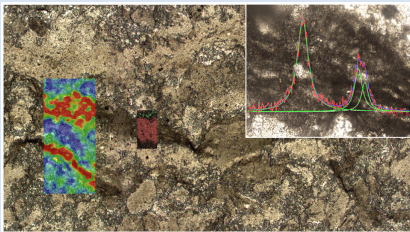# Correlative microspectroscopy of biogenic fabrics in Proterozoic silicified stromatolites

K. Hickman-Lewis[1,2,a]*, B. Cavalazzi[2,3], W. Montgomery[1]

OPEN ACCESS

Abstract

https://doi.org/10.7185/geochemlet.2419

Questions surrounding the biogenicity of ancient stromatolites have perplexed geobiologists for decades. Abiotic processes can produce superficially stromatolite-like structures; moreover, stromatolites frequently fail to preserve organic materials and cellular traces of their microbial architects. Using spatially correlated optical and electron microscopy coupled with Raman and FTIR microspectroscopy, we show that silicified stromatolites from the Tonian Skillogalee Dolomite (Flinders Ranges, South Australia) contain exceptionally well preserved microbial mat fragments and microbially induced sedimentary structures. These organic-rich layers exhibit mat-like laminations with low degrees of inheritance and reflect interactions between microbial communities and their environments, *i.e.* growth, sediment trapping and binding, and reactions to early diagenesis, and are inconsistent with abiotic formation. Although accounting for a minor proportion of the volume of the stromatolites, these kerogenous relics are demonstrably syngenetic and comprise aromatic and aliphatic organic materials, likely preserved due to early and rapid silicification. Constraining the origins of such lamination-scale features can elucidate relationships between morphogenesis and diagenesis and may assist in the resolution of controversies surrounding stromatolite biogenicity in deep time.

Introduction

Stromatolites are laminated organo-sedimentary structures archiving complex interplays between microbial mat growth, nutrient diffusion, sedimentation, mineral nucleation, and hydrological and geochemical regimes (Burne and Moore, 1987; Awramik, 2006; Hickman-Lewis et al., 2019). They provide a record of microbial ecosystems throughout almost 3.5 billion years of Earth history and are counted amongst the oldest traces of life (Awramik, 2006). Nonetheless, their geobiological significance is repeatedly challenged; indeed, Ginsburg (1991) stated that "almost everything about stromatolites has been, and remains to varying degrees, controversial." Despite numerous compelling lines of evidence pointing to the biogenic origins of most fossil stromatolite-like structures (Awramik, 2006; Schopf, 2006), doubts endure regarding the unambiguous identification of primary biological influence in ancient examples with diverse morphologies (Lowe, 1994; Grotzinger and Rothman, 1996; Perri et al., 2013; Brasier et al., 2019). It has been theoretically and experimentally demonstrated that abiotic processes can produce laminated *stromatoloids*, whose macrostructures mirror those of fossil stromatolites (Buick et al., 1981; Dupraz et al., 2006; McLoughlin et al., 2008); nonetheless, truly non-biological stromatolite-like features (*e.g.*, de Wit et al., 1982) are probably rare in the geological record.

Establishing biogenicity in ancient stromatolites is also hindered by a general lack of preservation of primary organic material and cellular microfossils (Buick et al., 1981). Kremer et al. (2012) noted that microfossil preservation in stromatolites is rare due to early post-mortem and diagenetic nanogranular calcification. Where present, organic materials in ancient stromatolites often occur as discrete particles or agglomerations, intermixed with other phases, that are impossible to associate with primary microbial communities, or as secondary, post-diagenetic hydrocarbon infiltration fabrics (Rasmussen et al., 2021).

In the absence of cellular preservation, lamination-scale mesostructural characteristics, *i.e.* at the scale of a well developed microbial community, could provide crucial evidence for biogenicity in ancient stromatolites with simple macrostructural morphologies. This contribution presents an example of such high fidelity preservation of organic materials within silicified carbonate stromatolites using a combination of textural, mineralogical, and spectroscopic observations that elucidate microbial mat growth processes and the preservational mechanisms of organic-rich biofabrics.

Geological Context

The studied stromatolites are from the Tonian Skillogalee Dolomite (Burra Group) at Prince Alfred copper mine, near Cradock, Flinders Ranges, South Australia (Figs. S-1, S-2) and date to ~790 Ma

1. The Natural History Museum, London, UK
2. Dipartimento BiGeA, Università di Bologna, Bologna, Italy
3. Department of Geology, University of Johannesburg, Johannesburg, South Africa
a. Current affiliation: Department of Earth Science and Engineering, Imperial College London, London, UK
*   Corresponding author (email: k.hickman-lewis@imperial.ac.uk)

(Preiss *et al.*, 2009). The mine is located at the east of the Nackara Arc where the Skillogalee Dolomite outcrops beneath an unconformity separating the pre-Sturtian Burra and post-Sturtian Umberatana groups (Preiss, 2000). Stromatolites from the Skillogalee Dolomite described by Preiss (1971, 1973) as *Baicalia burra* are now widely used in Neoproterozoic chronostratigraphy.

Palaeoenvironmental studies of the Skillogalee Dolomite conclude that it reflects a low energy peritidal setting associated with an inner platform reef (Preiss, 1971, 1973; Virgo *et al.*, 2021). Sr and O isotope systematics suggest marine deposition although certain horizons enriched in ^{18}O and ^{13}C denote intertidal–peritidal evaporitic episodes (Belperio, 1990). Coupling sedimentological observations with trace and rare earth element (REE) geochemistry, Virgo *et al.* (2021) identified ripple marks and desiccation structures, superchondritic Y/Ho, light REE depletion and positive Eu anomalies consistent with a dynamic shallow water environment featuring clastic input and simultaneous marine, intertidal and fluvial influences. Although interbedded magnesite-bearing horizons may represent palaeoenvironments that were largely inclement to life (Belperio, 1990), primary dolomitic horizons evince colonisation by stromatolite-forming communities (Preiss, 1971, 1973).

Results

The Skillogalee stromatolites feature stratiform–domical macro-structures comprising undulatory and laterally discontinuous layers (~0.5–2 mm) of micritic mudstone and packstone–boundstone (Figs. 1, S-3–S-6). Layers are primarily composed of fine grained dolomicrite and dolomicrospar (wackestone–packstone–boundstone), quartz, and rare cement-filled vugs and intraclasts (Figs. 1, S-3–S-6). SEM-EDS analyses show that, in addition to dolomite and quartz, aluminous phyllosilicates, pyrite, apatite and rare mafic phases occur throughout the matrix (Figs. 1, S-8–S-11). The stromatolites also feature organic-rich laminations with a low degree of inheritance, *i.e.* the topography of the underlying layers does not strongly act as a template for the overlying layers (Figs. 2d,e, S-4). Rare stylolites disconformably cross stromatolitic laminations (Fig. 1a,b). Some organic-rich laminations feature millimetre-scale (pseudo)columnar or microdomical structures (Figs. S-3, S-4 and S-6) whereas others include domains of organic-rich bindstone including fine, undulatory, wispy laminations set within a micrite/micrinite matrix (Figs. 1a,b, S-7). Isolated laminated organic fragments occur throughout the matrix (Fig. 1a,b). Many darker laminations are surrounded by pale brown–grey domains of diffuse organic material (Figs. 2c, S-7; organic staining *cf.* Pomoni and Karakitsios, 2016; DeMott *et al.*, 2020). High magnification optical microscopy indicates that these diffuse organic materials occur mostly within interstitial zones of a fine grained mineral matrix (Fig. S-7). Some laminae bind grains in a pliable manner denoting original plasticity; elsewhere, carbonate particles surrounded by poorly preserved laminae form networks of oriented grains suspended within an organic matrix (Fig. 2b).
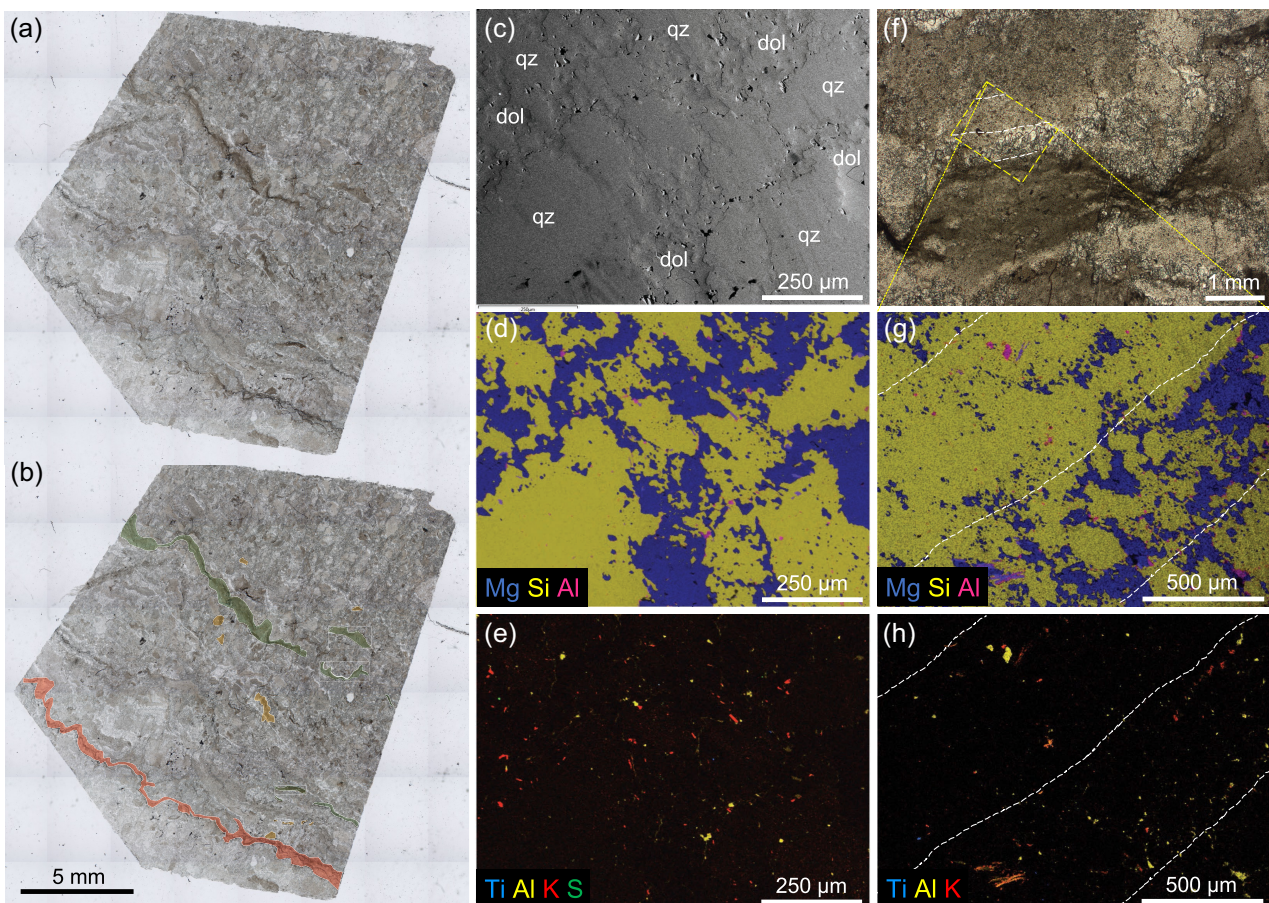

Figure 1 Petrographic characterisation of stromatolites in thin section. **(a, b)** Optical photomicrographs (original and annotated, respectively) showing organic-rich stromatolitic mesostructure (green), disseminated organics (amber) and stylolite (red). **(c–e)** SEM image and EDS maps showing representative matrix fabric; dol = dolomite, qz = quartz. **(f–h)** Optical photomicrograph **(f)** and EDS maps **(g, h)** showing contact between organic-rich layer and matrix.
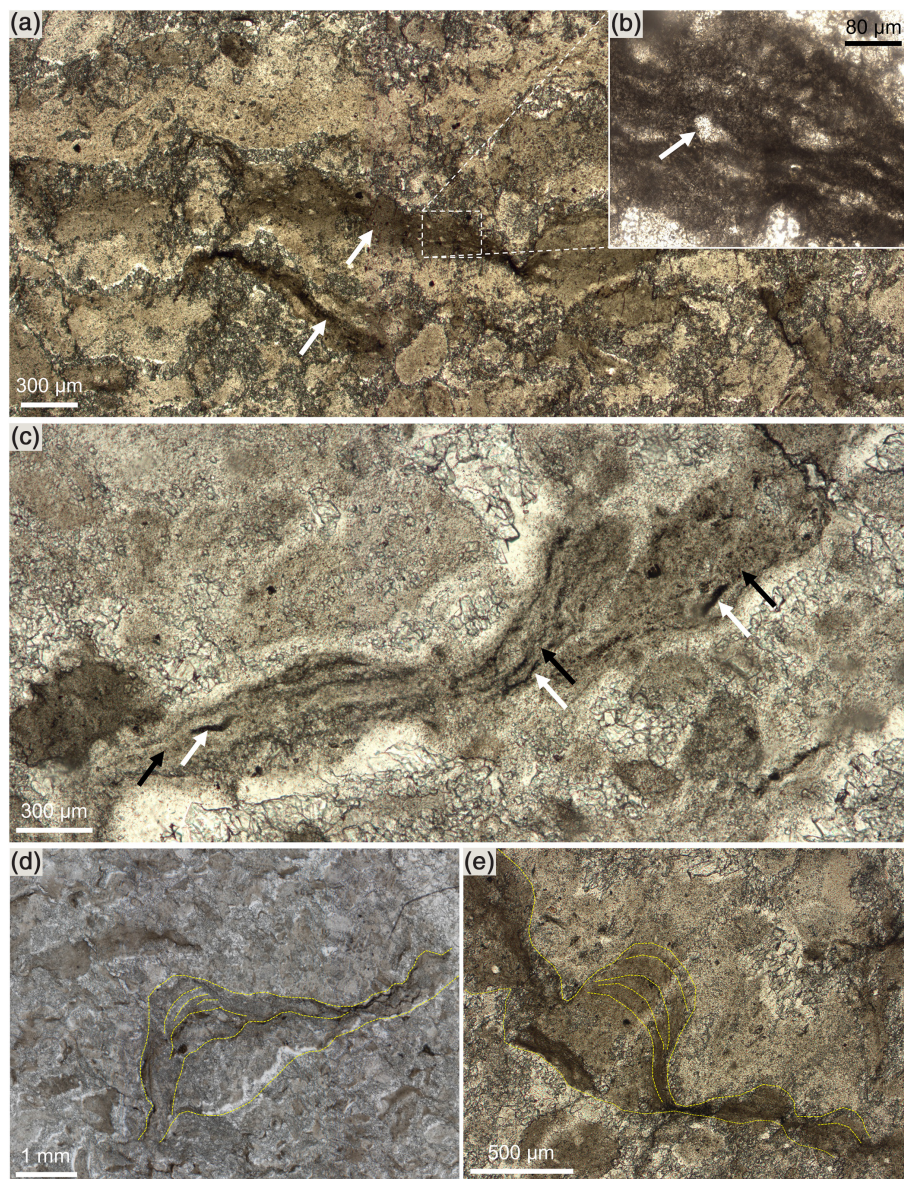
Figure 2 Thin section optical photomicrographs showing organic fabrics. **(a, b)** Undulatory organic-rich layers (arrows) containing oriented particles (inset **(b)**, arrow). **(c)** Organic-rich layer featuring mat laminae (white arrows) surrounded by pale brown–grey organic staining (black arrows). **(d, e)** Biogenic stromatolitic laminations exhibiting a low–medium degree of inheritance; dotted lines trace visible stromatolitic laminations.

Raman microspectroscopy was used to map the distribution of carbonaceous materials and mineral phases associated with organic-rich laminations (Fig. 3a–d). The matrix is dominated by dolomite (Raman peaks at 175, 300, 723 and 1095 cm^{-1}) and quartz (peaks at 205 and 465 cm^{-1}), whereas the laminations are richer in carbonaceous materials (peaks at ~1340 and ~1600 cm^{-1}). Quartz is often concentrated in layers surrounding carbonaceous materials (Fig. 3c). Although some carbonaceous materials show weak layering (Fig. 3d), most occur as diffuse clouds (Fig. S-12d). Raman geothermometry using carbonaceous materials-based spectral deconvolution was applied to organic-rich laminations to determine peak metamorphic temperatures (Fig. 3e, Table S-1); peak thermal histories of 348 ± 50 °C (after Beyssac *et al.*, 2002), and 346 ± 30 °C and 317 ± 50 °C (after Kouketsu *et al.*, 2014) were calculated.

FTIR microspectroscopy was used to identify and map functional groups within the organic-rich laminations (Fig. 4, Table S-2). In the aliphatic stretching region (3000–2800 cm^{-1};

Fig. 4d), methylene CH$_2$, terminal-methyl CH$_3$ and alkene =C–H moieties were detected in both stromatolitic laminations and the surrounding domains of diffuse organic materials. Weak signals potentially attributable to methyne C–H were also detected in laminations. Mapping both aliphatic C–H (2850 cm^{-1}) and aromatic C=C (1600 cm^{-1}) stretches shows more intense detections within dark carbonaceous laminations and a very low abundance or absence in the surrounding matrix (Fig. 4a–c); weak organic detections occur disseminated within fine grained dolomicrospar but are absent within dolosparite (Fig. 3). Although C–H and C=C detections are strongest in dark carbonaceous laminations, a weaker 'halo'-like signal is also present in the surrounding diffuse organic staining domains (Figs. 4, S-13).

Discussion

A serious impediment to establishing the biogenic origins of Precambrian carbonate stromatolites is the absence of preserved
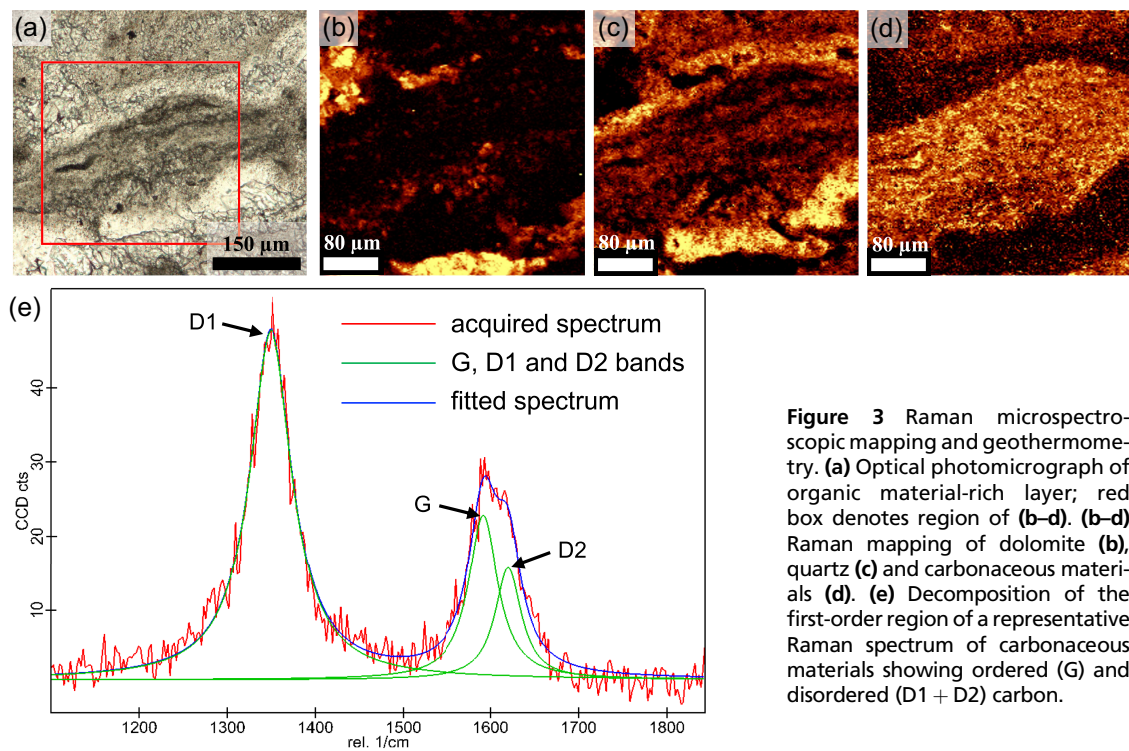
Figure 3 Raman microspectroscopic mapping and geothermometry. **(a)** Optical photomicrograph of organic material-rich layer; red box denotes region of **(b–d)**. **(b–d)** Raman mapping of dolomite **(b)**, quartz **(c)** and carbonaceous materials **(d)**. **(e)** Decomposition of the first-order region of a representative Raman spectrum of carbonaceous materials showing ordered (G) and disordered (D1 + D2) carbon.

cellular and cell-associated organic materials and biofabrics. Stromatolites from the Skillogalee Dolomite exhibit exceptional preservation of organic material-rich laminations interpreted to represent microbial mats and microbially induced sedimentary structures (MISS); their lithofacies association implies authigenic microbialite growth on a carbonate platform and is consistent with palaeoenvironmental interpretations (Virgo *et al.*, 2021).

By performing the first correlated optical, SEM-EDS, Raman and FTIR microanalyses of microbial mat structures in Precambrian carbonate stromatolites, we have shown systematic spatial variations in the signatures of organic and mineral phases throughout the microbial stratigraphy of *Baicalia burra* from the Tonian Skillogalee Dolomite that illuminate the morphogenetic and diagenetic history of these stromatolites.

The morphology of kerogen-rich layers is diagnostic of microbial mat growth. Non-isopachous laminations exhibiting a poor degree of inheritance are consistent with laterally variable biomass productivity and suggest complex interactions between ecosystems and local palaeoenvironments, which manifest as numerous directionally conflicting growth and decay morphogenetic vectors (Dupraz *et al.*, 2006; Hickman-Lewis *et al.*, 2019). Low degrees of inheritance are most common in regions containing organic material-rich laminations (Figs. 2d,e, S-4), here interpreted to be biogenic, *i.e.* the growth of the stromatolite-building community provided new relief, seeding topographic complexity that resulted in a sequence of layers characterised by low degrees of inheritance. Layers with a higher degree of inheritance are typically poorer in, or devoid of, organic materials, and we therefore suggest that these feature minimal biological morphogenetic components. The presence of isolated fragments of laminated organic materials in the matrix (Fig. 1a,b) may indicate either poorly formed mats or the reworking of epibenthic mats under energetic hydrodynamic regimes (Noffke *et al.*, 2001, 2022). Sub-angular carbonate particles bound within laminae (Figs. 2b, S-12) have a plausible origin through microbially mediated carbonate precipitation under

carbonate-supersaturated Neoproterozoic interglacial conditions (Hood and Wallace, 2012; Corkeron and Slezak, 2020). The orientation of these particles parallel to mat layers can be explained as an MISS: silt grade sediment baffled by vertically oriented microbial filaments was captured within upward-growing microbial biofilms, before becoming entrapped within the fossilised mat, which pushes the grains apart during biofilm growth (Noffke *et al.*, 1997, 2001).

The dominance of aromatic moieties in Raman and FTIR microspectroscopic data (Figs. 3, 4) indicate that the kerogen composing organic laminations is thermally mature. Its peak thermal maturity (317–348 °C) is consistent with the metamorphic history of the region (greenschist facies; Preiss, 1971), strongly suggesting that the kerogen derives from primary stromatolite-building communities. Furthermore, weak but unambiguous signals from aliphatic compounds in FTIR spectra, although providing only a qualitative estimation of maturity, suggest that moderate pressures and temperatures have influenced the kerogen, consistent with the quantitative estimation of thermal history from Raman data. Correlated microspectroscopic data therefore show that the mesostructures of interest are neither purely graphitic nor entirely aromatic, but retain a small amount of primary aliphatic complexity, *i.e.* moderately thermally mature carbonaceous materials. The syngeneity of kerogen is further supported by domains of diffuse organic staining surrounding dark laminations (Fig. S-7), indicating early diagenetic micro-scale mixing of fluids rich in finely particulate organic matter (Hips *et al.*, 2011); such domains are known to develop from early dissolution–reprecipitation of primary organic matter (DeMott *et al.*, 2020). The strong localisation of kerogen within microbial mat structures and its absence from matrix fractures renders secondary hydrocarbon contamination implausible.

The preservation of organic materials in these carbonate stromatolites can be explained by their early post-depositional history. The presence of microquartz immediately surrounding organic-rich layers and more broadly throughout the matrix
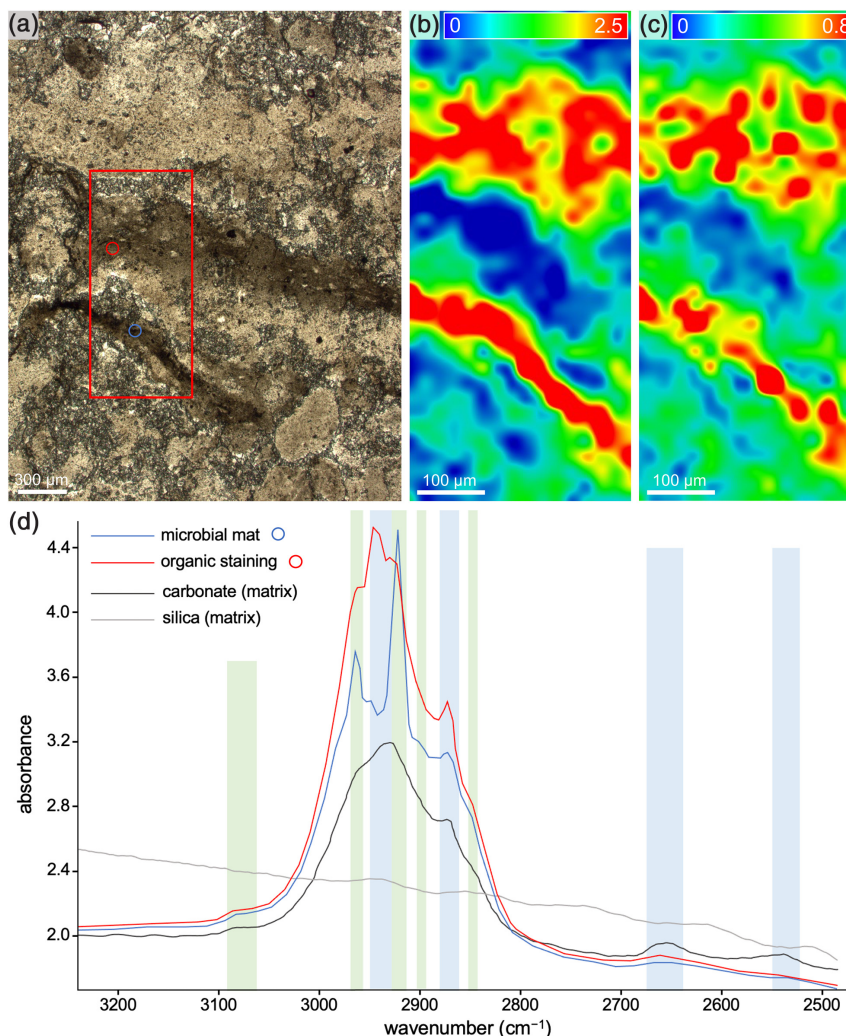
Figure 4 FTIR microspectroscopic characterisation of organic materials. **(a)** Optical photomicrograph of organic material-rich layer; red box denotes region of **(b, c)**. **(b, c)** FTIR intensity maps for the C=C band at ~1600 cm^{-1} **(b)**, and C–H band at ~2850 cm^{-1} **(c)**. Colour scales given in absorbance units. **(d)** Representative FTIR spectra showing peaks corresponding to organic materials (green) and carbonate (blue). Spectra from matrix carbonate and silica are provided for comparison.

(Figs. 1, 3) suggests a palaeodepositional environment super-saturated with respect to silica, which precipitated rapidly, *i.e.* the earliest diagenetic processes included penecontemporaneous silicification. As in more ancient fossil microbialites, we interpret this early and rapid silica precipitation as contributing to the exceptional preservation of biochemical heterogeneity in the otherwise labile organic fraction; such preservation is otherwise rare in carbonates (Kremer *et al.*, 2012).

Although constraining the origins of ancient stromatolite-like structures is challenging, demonstrably syngenetic mature organic materials exhibiting spatial distributions consistent with microbial morphogenesis and spectral characteristics consistent with thermally altered biological organic materials can allow biogenicity to be established. Such occurrences can be considered fossil *lagerstätten*. Identifying similar mesoscale phenomena in more ancient stromatolites using the correlated imaging–microspectroscopy approach developed herein could facilitate definitive interpretations of their morphogenesis.

Acknowledgements

Editor: Liane G. Benning

Additional Information

Cite this letter as: Hickman-Lewis, K., Cavalazzi, B., Montgomery, W. (2024) Correlative microspectroscopy of

biogenic fabrics in Proterozoic silicified stromatolites. *Geochem. Persp. Let.* 30, 34–39. https://doi.org/10.7185/geochemlet.2419

References

Awramik, S.M. (2006) Respect for stromatolites. *Nature* 441, 700–701. https://doi.org/10.1038/441700a

Belperio, A.P. (1990) Palaeoenvironmental interpretation of the Late Proterozoic Skillogalee Dolomite in the Willouran Ranges, South Australia. In: Jago, J.V., Moore, P.J. (Eds.) *The Evolution of a Late Precambrian-Early Palaeozoic Rift Complex: The Adelaide Geosyncline.* Special Publication 16, Geological Society of Australia, Sydney, 85–104.

Beyssac, O., Goffé, B., Chopin, C., Rouzaud, J.N. (2002) Raman spectra of carbonaceous material in metasediments: a new geothermometer. *Journal of Metamorphic Geology* 20, 859–871. https://doi.org/10.1046/j.1525-1314.2002.00408.x

Brasier, A.T., Dennis, P.F., Still, J., Parnell, J., Culwick, T., Brasier, M.D., Wacey, D., Bowden, S.A., Crook, S., Boyce, A.J., Muirhead, D.K. (2019) Detecting ancient life: Investigating the nature and origin of possible stromatolites and associated calcite from a one billion year old lake. *Precambrian Research* 328, 309–320. https://doi.org/10.1016/j.precamres.2019.04.025

Buick, R., Dunlop, J.S.R., Groves, D.I. (1981) Stromatolite recognition in ancient rocks: an appraisal of irregularly laminated structures in an Early Archaean chert-barite unit from North Pole, Western Australia. *Alcheringa* 5, 161–181. https://doi.org/10.1080/03115518108566999

Burne, R.V., Moore, L.S. (1987) Microbialites; organosedimentary deposits of benthic microbial communities. *Palaios* 2, 241–254. https://doi.org/10.2307/3514674

Corkeron, M.L., Slezak, P.R. (2020) Stromatolite framework builders: ecosystems in a Cryogenian interglacial reef. *Australian Journal of Earth Sciences* 67, 833–856. https://doi.org/10.1080/08120099.2020.1732464

DeMott, L.M., Napieralski, S.A., Junium, C.K., Teece, M., Scholz, C.A. (2020) Microbially influenced lacustrine carbonates: A comparison of Late Quaternary Lahontan tufa and modern thrombolite from Fayetteville Green Lake, NY. *Geobiology* 18, 93–112. https://doi.org/10.1111/gbi.12367

de Wit, M.J., Hart, R., Martin, A., Abbott, P. (1982) Archean abiogenic and probable biogenic structures associated with mineralized hydrothermal vent systems and regional metasomatism, with implications for greenstone belt studies. *Economic Geology* 77, 1783–1802. https://doi.org/10.2113/gsecongeo.77.8.1783

Dupraz, C., Pattisina, R., Verrecchia, E.P. (2006) Translation of energy into morphology: Simulation of stromatolite morphospace using a stochastic model. *Sedimentary Geology* 185, 185–203. https://doi.org/10.1016/j.sedgeo.2005.12.012

Ginsburg, R.N. (1991) Controversies about stromatolites: vices and virtues. In: Müller, D.W., McKenzie, J.A., Weissert, H. (Eds.) *Controversies in Modern Geology.* Academic Press, London, 25–36.

Grotzinger, J.P., Rothman, D.H. (1996) An abiotic model for stromatolite morphogenesis. *Nature* 383, 423–425. https://doi.org/10.1038/383423a0

Hickman-Lewis, K., Gautret, P., Arbaret, L., Sorieul, S., De Wit, R., Foucher, F., Cavalazzi, B., Westall, F. (2019) Mechanistic Morphogenesis of Organo-Sedimentary Structures Growing Under Geochemically Stressed Conditions: Keystone to Proving the Biogenicity of Some Archaean Stromatolites? *Geosciences* 9, 359. https://doi.org/10.3390/geosciences9080359

Hips, K., Haas, J., Vidó, M., Barna, Z., Jovanović, D., Sudar, M.N., Siklósy, Z. (2011) Selective blackening of bioclasts via mixing-zone aragonite neomorphism in Late Triassic limestone, Zlatibor Mountains, Serbia. *Sedimentology* 58, 854–877. https://doi.org/10.1111/j.1365-3091.2010.01186.x

Hood, A.v.S., Wallace, M.W. (2012) Synsedimentary diagenesis in a Cryogenian reef complex: Ubiquitous marine dolomite precipitation. *Sedimentary Geology* 255–256, 56–71. https://doi.org/10.1016/j.sedgeo.2012.02.004

Kouketsu, Y., Mizukami, T., Mori, H., Endo, S., Aoya, M., Hara, H., Nakamura, D., Wallis, S. (2014) A new approach to develop the Raman carbonaceous material geothermometer for low-grade metamorphism using peak width. *Island Arc* 23, 33–50. https://doi.org/10.1111/iar.12057

Kremer, B., Kazmierczak, J., Łukomska-Kowalczyk, M., Kempe, S. (2012) Calcification and Silicification: Fossilization Potential of Cyanobacteria from Stromatolites of Niuafo'ou's Caldera Lakes (Tonga) and Implications for the Early Fossil Record. *Astrobiology* 12, 535–548. https://doi.org/10.1089/ast.2011.0742

Lowe, D.R. (1994) Abiological origin of described stromatolites older than 3.2 Ga. *Geology* 22, 387–390. https://doi.org/10.1130/0091-7613(1994)022<0387:AOODSO>2.3.CO;2

McLoughlin, N., Wilson, L.A., Brasier, M.D. (2008) Growth of synthetic stromatolites and wrinkle structures in the absence of microbes – implications for the early fossil record. *Geobiology* 6, 95–105. https://doi.org/10.1111/j.1472-4669.2007.00141.x

Noffke, N., Gerdes, G., Klenke, T., Krumbein, W.E. (1997) A microscopic sedimentary succession of graded sand and microbial mats in modern siliciclastic tidal flats. *Sedimentary Geology* 110, 1–6. https://doi.org/10.1016/S0037-0738(97)00039-0

Noffke, N., Gerdes, G., Klenke, T., Krumbein, W.E. (2001) Microbially Induced Sedimentary Structures: A New Category within the Classification of Primary Sedimentary Structures. *Journal of Sedimentary Research* 71, 649–656. https://doi.org/10.1306/2DC4095D-0E47-11D7-8643000102C1865D

Noffke, N., Beraldi-Campesi, H., Callefo, F., Carmona, N.B., Cuadrado, D.G., Hickman-Lewis, K., Homann, M., Mitchell, R., Sheldon, N., Westall, F., Xiao, S. (2022) Microbially Induced Sedimentary Structures (MISS). *Treatise Online* 162, Part B, Volume 2, Chapter 5, 1–29.

Perri, E., Tucker, M.E., Mawson, M. (2013) Biotic and Abiotic Processes In the Formation and Diagenesis of Permian Dolomitic Stromatolites (Zechstein Group, NE England). *Journal of Sedimentary Research* 83, 896–914. https://doi.org/10.2110/jsr.2013.65

Pomoni, F.A., Karakitsios, V. (2016) Sedimentary facies analysis of a high-frequency, small-scale, peritidal carbonate sequence in the Lower Jurassic of the Tripolis carbonate unit (central western Crete, Greece): Long-lasting emergence and fossil laminar dolocretes horizon. *Journal of Palaeogeography* 5, 241–257. https://doi.org/10.1016/j.jop.2016.05.003

Preiss, W.V. (1971) The biostratigraphy and palaeoecology of South Australian Precambrian stromatolites. Ph.D. Thesis, University of Adelaide.

Preiss, W.V. (1973) Palaeoecological interpretations of South Australian Precambrian stromatolites. *Journal of the Geological Society of Australia* 19, 501–532. https://doi.org/10.1080/00167617308728820

Preiss, W.V. (2000) The Adelaide Geosyncline of South Australia and its significance in Neoproterozoic continental reconstruction. *Precambrian Research* 100, 21–63. https://doi.org/10.1016/S0301-9268(99)00068-6

Preiss, W.V., Drexel, J.F., Reid, A.J. (2009) Definition and age of the Kooringa Member of the Skillogalee Dolomite: host for Neoproterozoic (c. 790 Ma) porphyry-related copper mineralisation at Burra. *MESA Journal* 55, 19–33.

Rasmussen, B., Muhling, J.R., Fischer, W.W. (2021) Ancient Oil as a Source of Carbonaceous Matter in 1.88-Billion-Year-Old Gunflint Stromatolites and Microfossils. *Astrobiology* 21, 655–672. https://doi.org/10.1089/ast.2020.2376

Schopf, J.W. (2006) Fossil evidence of Archaean life. *Philosophical Transactions of the Royal Society B* 361, 869–885. https://doi.org/10.1098/rstb.2006.1834

Virgo, G.M., Collins, A.S., Amos, K.J., Farkaš, J., Blades, M.L., Subarkah, D. (2021) Descending into the "snowball": High resolution sedimentological and geochemical analysis across the Tonian to Cryogenian boundary in South Australia. *Precambrian Research* 367, 106449. https://doi.org/10.1016/j.precamres.2021.106449

Correlative microspectroscopy of biogenic fabrics in Proterozoic silicified stromatolites

K. Hickman-Lewis, B. Cavalazzi, W. Montgomery

Supplementary Information

The Supplementary Information includes:

- ➤ Experimental Protocols
- ➤ Tables S-1 and S-2
- ➤ Figures S-1 to S-14
- ➤ Supplementary Information References

Experimental Protocols

1. Samples and subsamples

The samples utilised for this research are part of the Martin Brasier Collection housed at the Oxford University Museum of Natural History, Oxford, United Kingdom. Six thin sections were imaged and studied using optical microscopy, from which three thin sections were chosen for further analysis based on the presence of mesoscale organic-rich laminations within. Organic-rich laminations were selected as regions of interest for geochemical study using SEM-EDX and Raman and FTIR microspectroscopy.

2. Optical microscopy

Transmitted and cross-polarised light optical photomicrographs were acquired using Leica Axio Scope.A1 (OUMNH, Oxford) and Olympus BX63 (NHM, London) microscopes. Images were acquired at magnifications between 20× and 1000× and captured using ZEN and CellSens software.

3. Scanning electron microscopy and energy-dispersive X-ray spectroscopy

SEM-EDS was undertaken using a JEOL JSM-IT 500 variable pressure SEM equipped with an Oxford Instruments X-Max EDS detector at the Natural History Museum (NHM), London. EDS maps were acquired at an accelerating voltage of 15 kV for 120 minutes. EDS spot analyses were acquired at an accelerating voltage of 15 kV for 180 s. Data were acquired and processed using AZtec software (Oxford Instruments).

4. Raman microspectroscopy

Raman maps were acquired using a WITec Confocal Raman microscope alpha300R system at the BiGeA Raman Laboratory, Università di Bologna. The Raman signal was collected using a 100× (numerical aperture of 0.90) objective (Nikon, Tokyo, Japan) and an average laser intensity of 5 mW at a depth beneath the thin section surface of 5 µm. Prior to analysis, samples were cleaned with isopropyl alcohol then with ultra-pure water. Scans were performed using a frequency-doubled Nd-YAG laser (Newport, Evry, France) providing excitation at a wavelength of 532 nm perpendicular to the sample surface to acquire confocal 2D (*x-y*) Raman maps. Data acquisition, evaluation and processing were performed using the WITec Project Management and Image Project Plus software suite.

Spectral deconvolution and Raman geothermometry was conducted using the carbonaceous material-based geothermometers developed by Beyssac *et al.* (2002) and Kouketsu *et al.* (2014). The Raman signal was again collected using a 100× (numerical aperture of 0.90) objective (Nikon, Tokyo, Japan) and an average laser intensity of 5 mW at a depth beneath the thin section surface of 5 µm. Peak metamorphic temperatures were determined as follows:

1) $T = -445 \times R2 + 641$ (Beyssac *et al.*, 2002),
2) $T = -2.15 \times (FWHM\text{-}D1) + 478$ (Kouketsu *et al.*, 2014),
3) $T = -6.78 \times (FWHM\text{-}D2) + 535$ (Kouketsu *et al.*, 2014),

where FWHM-D1 and FWHM-D2 denote the full width half maxima of the D1 and D2 bands, respectively. Equation 1 is valid in the temperature range 330–700 °C; Equations 2 and 3 are valid in the temperature range 165–655 °C.

5. Fourier transform infra-red (FTIR) microspectroscopy

FTIR spectral maps were obtained using a Nicolet iN10 mx FTIR microscope (ThermoFisher Scientific) at the Imaging and Analysis Centre, NHM London. The aperture was set to 50 µm × 50 µm. Maps covered the areas of interest with a grid spacing of 50 µm in both axes. Spectra were collected from 4000–675 cm^{-1} with a spectral resolution of 4 cm^{-1} using a liquid nitrogen-cooled MCT/A detector and a KBr beamsplitter. For maps, each spectrum was collected for 19.73 seconds (64 scans). A background spectrum with the same parameters was collected through air every 20 minutes.

Single spectra (reported in Fig. 4D) were acquired for 78.92 s (256 scans) with the aperture set to 50 µm × 50 µm. A background spectrum with the same parameters was collected through air prior to each single spectrum acquisition. Data were acquired and processed using OmnicPicta software (ThermoFisher Scientific).

Supplementary Tables

Table S-1   Peak thermal histories determined by Raman geothermometry.

Geothermometer	Peak temperature	Range of validity of geothermometer
$T = -445 \times R2 + 641$ (Beyssac *et al.*, 2002)	348 ± 50 °C	330–700 °C
$T = -2.15 \times (\text{FWHM-D1}) + 478$ (Kouketsu *et al.*, 2014)	346 ± 30 °C	165–655 °C
$T = -6.78 \times (\text{FWHM-D2}) + 535$ (Kouketsu *et al.*, 2014)	317 ± 50 °C	165–655 °C

Table S-2   Peak identifications in FTIR spectra. See Figure 4d for representative FTIR spectra.

Wavenumber (cm^{-1})	Designation
2500–2700	Carbonate (dolomite)
2850	Symmetrical CH_2 stretch
2870	Carbonate (dolomite?)
2895	Methyne C–H stretch (?)
2920	Asymmetrical CH_2 stretch
2940	Carbonate (dolomite)
2960	Asymmetrical CH_3 stretch
3080	Alkene =C–H stretch

Supplementary Figures
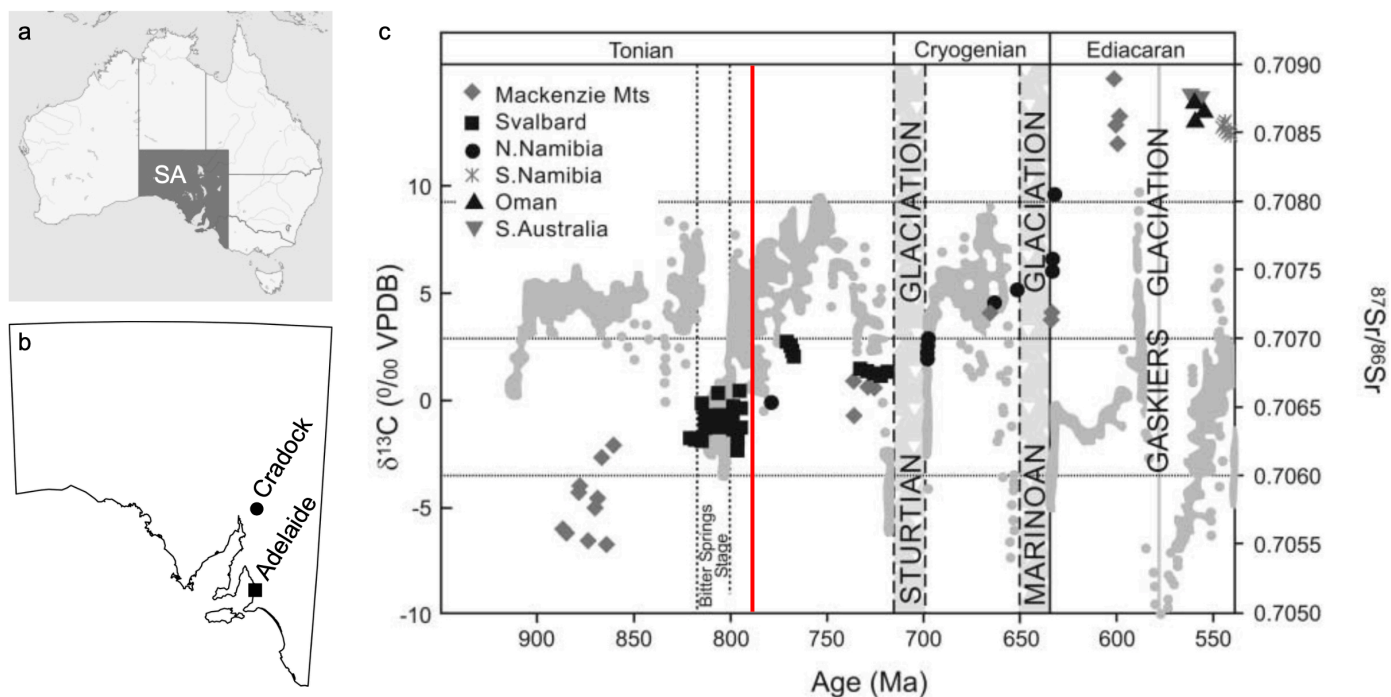
Figure S-1   Geographical and geochronological context of the Skillogalee Dolomite. **(a, b)** Locality information; the Skillogalee Dolomite samples studied were sourced from the Prince Alfred copper mine, near Cradock, South Australia (SA). **(c)** Geological timescale showing the evolution of carbonate $\delta^{13}C$ (grey symbols) and $^{87}Sr/^{86}Sr$ (black symbols) throughout the Neoproterozoic; the red line indicates the estimated age of the Skillogalee Dolomite (~790 Ma), *i.e.* during the period between the Bitter Springs Stage and the Sturtian Glaciation. Panel **(c)** is adapted from Fairchild and Kennedy (2007).

Figure S-2 Simplified stratigraphy and palaeoenvironmental reconstruction of the Tonian–Cryogenian transition in the Central Flinders Ranges. Samples were obtained from the upper Skillogalee Dolomite at the Prince Alfred copper mine near Cradock, South Australia (note that the unconformity at this locality precludes identifying the approximate stratigraphic height and horizon from which the stromatolites were sampled). Formations listed in grey text at the Tonian–Cryogenian transition do not occur at the Prince Alfred copper mine, where an unconformity separates the underlying Skillogalee Dolomite from the overlying Tapley Hill Formation. Stratigraphy adapted from Preiss (1971, 2000), Preiss *et al.* (1998), Fromhold and Wallace (2012) and Virgo *et al.* (2021). The *y*-axis is proportional to neither thickness nor time.

Figure S-3 Optical photomicrograph of thin section of Skillogalee Dolomite exhibiting silicified stromatolitic structures. Sample PM66-5. Organic-rich layers appear brown-grey in colour. Field of view is ~2 cm. Potential micro-domical biogenic features, which may represent the incipient growth of microbial domes, are arrowed.
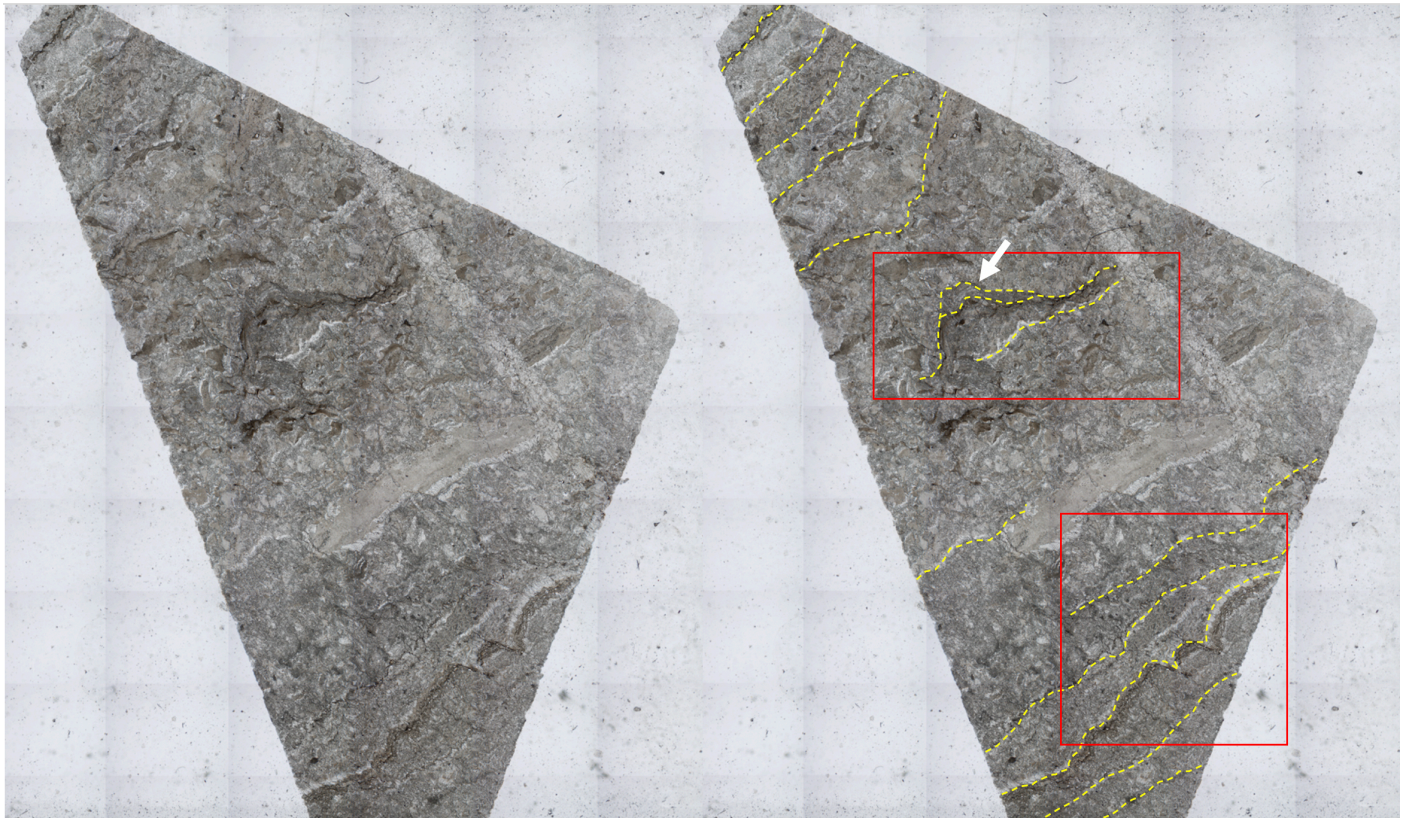
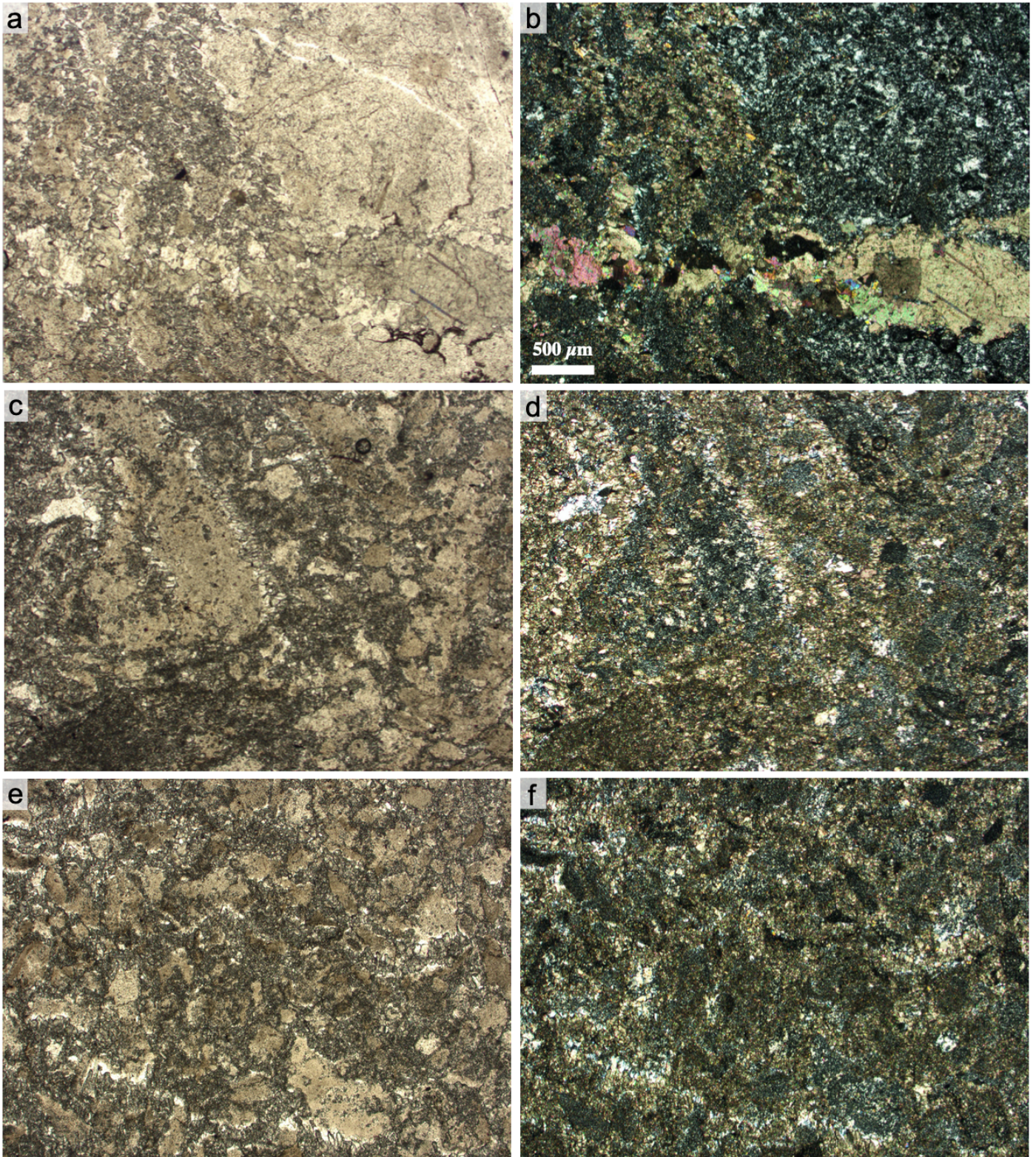**Figure S-4**   Optical photomicrograph mosaics of thin section of Skillogalee Dolomite exhibiting silicified stromatolitic structures. Sample PM66-5. Organic-rich layers appear brown-grey in colour. Field of view for each photomicrograph mosaic is ~2 cm. Potential micro-domical biogenic features, which may represent the incipient growth of microbial domes, are arrowed.

Figure S-5   Representative optical photomicrographs showing matrix carbonate fabrics (dolomite + quartz + oxides + oxyhydroxides) in the Skillogalee Dolomite stromatolites. Left-hand column shows images taken in plane polarised light; right-hand column shows images taken under cross-polarised light. Scale bar in **(b)** applies to all images.
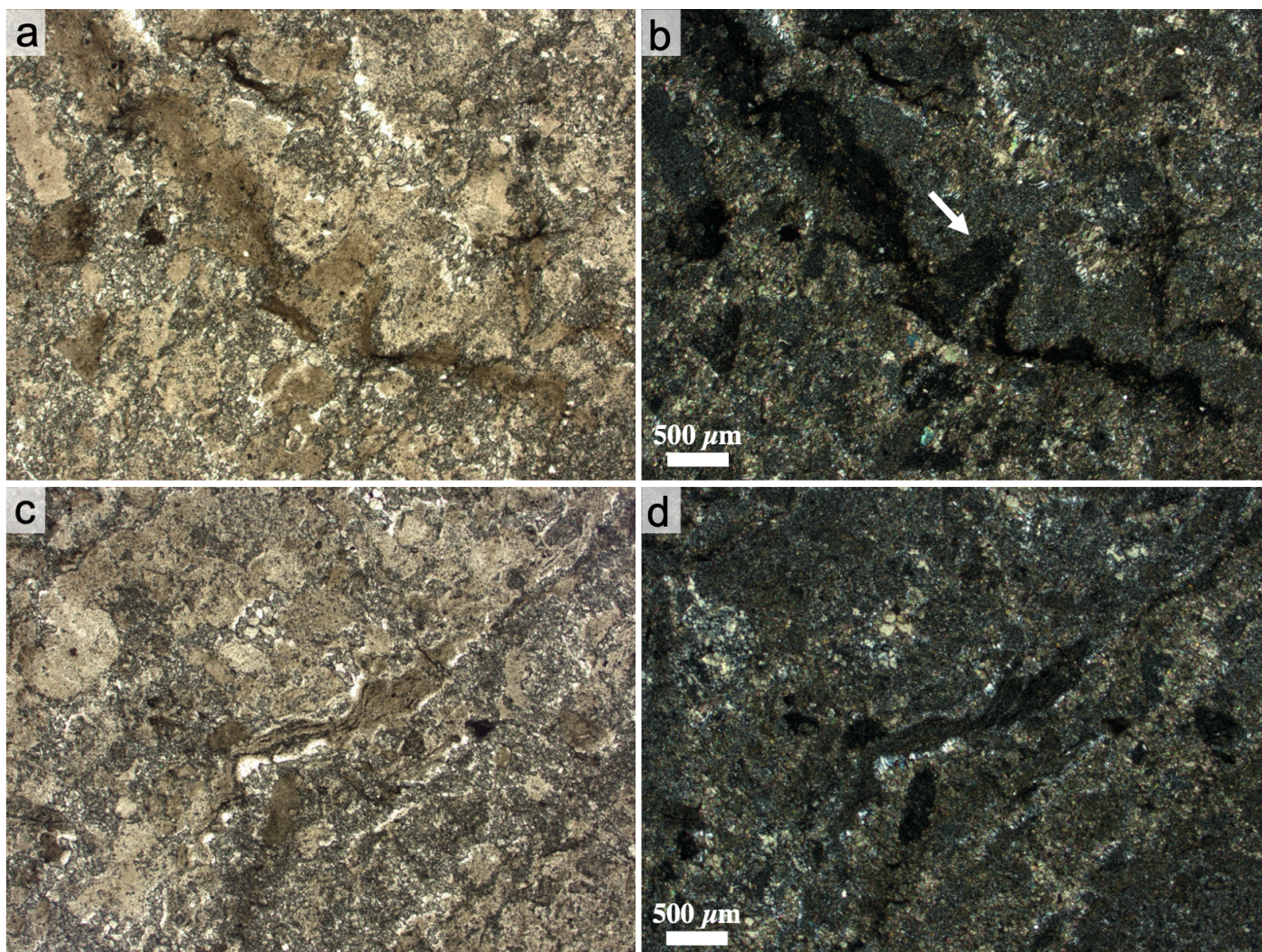
Figure S-6   Optical microscopy observations of organic material-rich laminations in the Skillogalee Dolomite stromatolites. **(a, b)** Organic-rich layer featuring columnar(?) structure. **(c, d)** Non-isopachous, weakly layered organic-rich layer. Plane polarised **(a, c)** and cross polarised **(b, d)** light images are shown. Scale bars in **(b)** and **(d)** apply to **(a)** and **(c)**, respectively. A potential columnar/pseudocolumnar biogenic feature, which may represent the incipient growth of microbial topographic complexity, is arrowed.
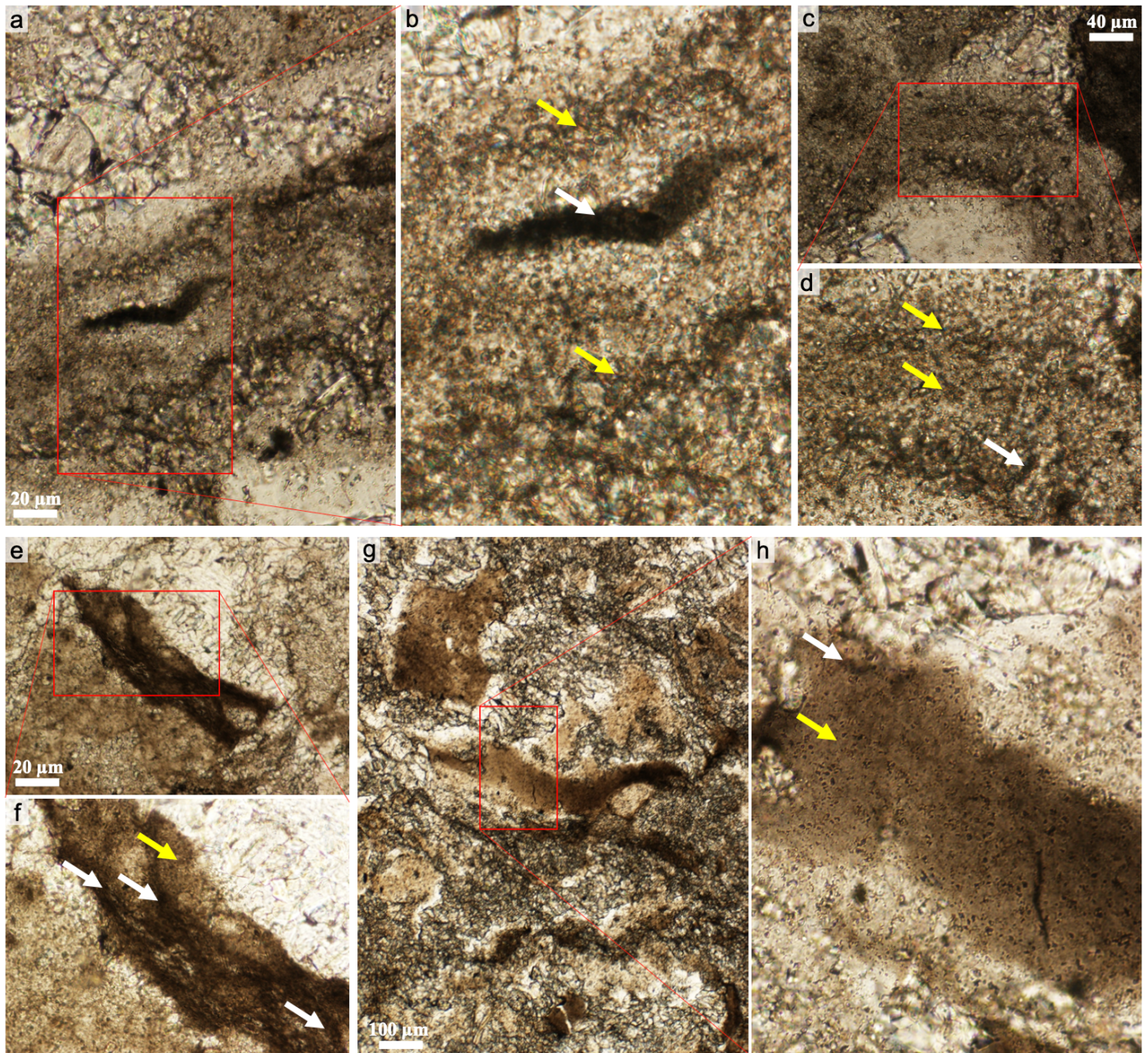
Figure S-7   High-resolution optical microscopy observations of organic laminations and regions of organic staining in stromatolitic laminations. **(a, b)** Laminated organic materials featuring carbonaceous wisps surrounded by pale grey-brown regions of organic staining. **(c, d)** Weakly laminated organic materials surrounded by regions of organic staining. **(e, f)** Laminated organic fragment. **(g, h)** Region of organic staining. White arrows throughout the figure denote primary carbonaceous laminations and fragments; yellow arrows denote regions of organic staining.
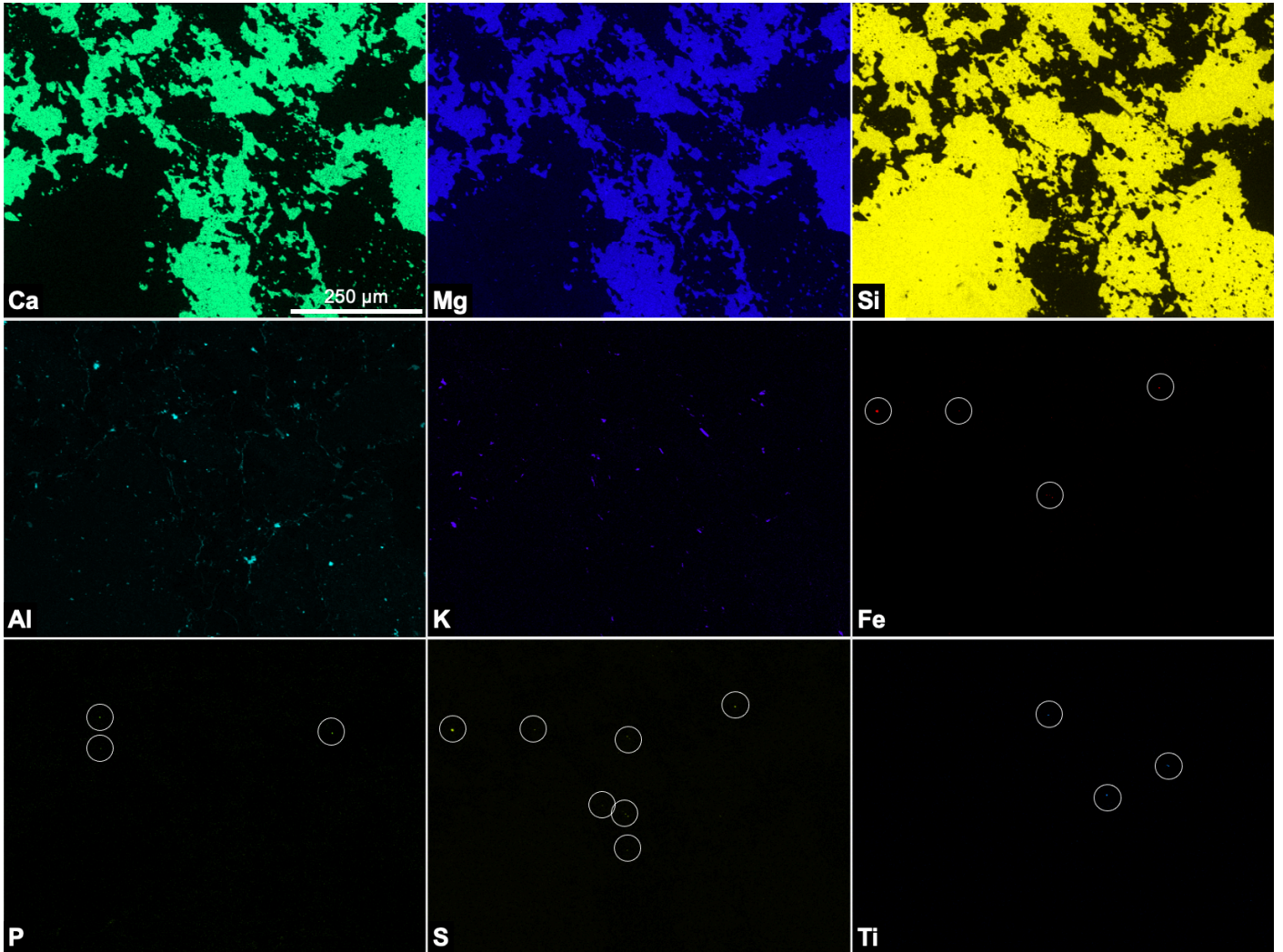
Figure S-8 Complete set of EDS elemental maps corresponding to the region of interest shown in Figure 1c–e.
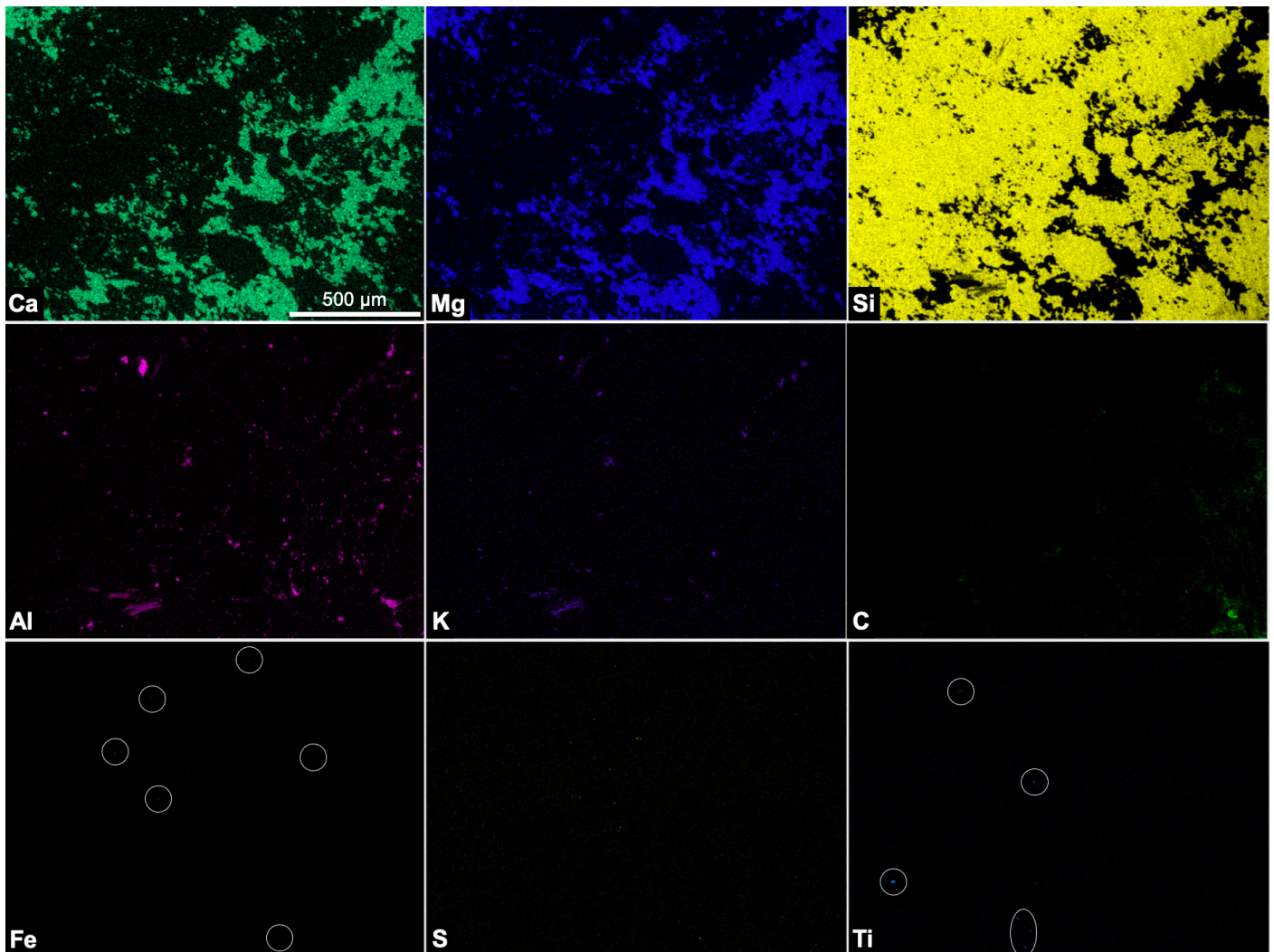
Figure S-9   Complete set of EDS elemental maps corresponding to the region of interest shown in Figure 1f–h.
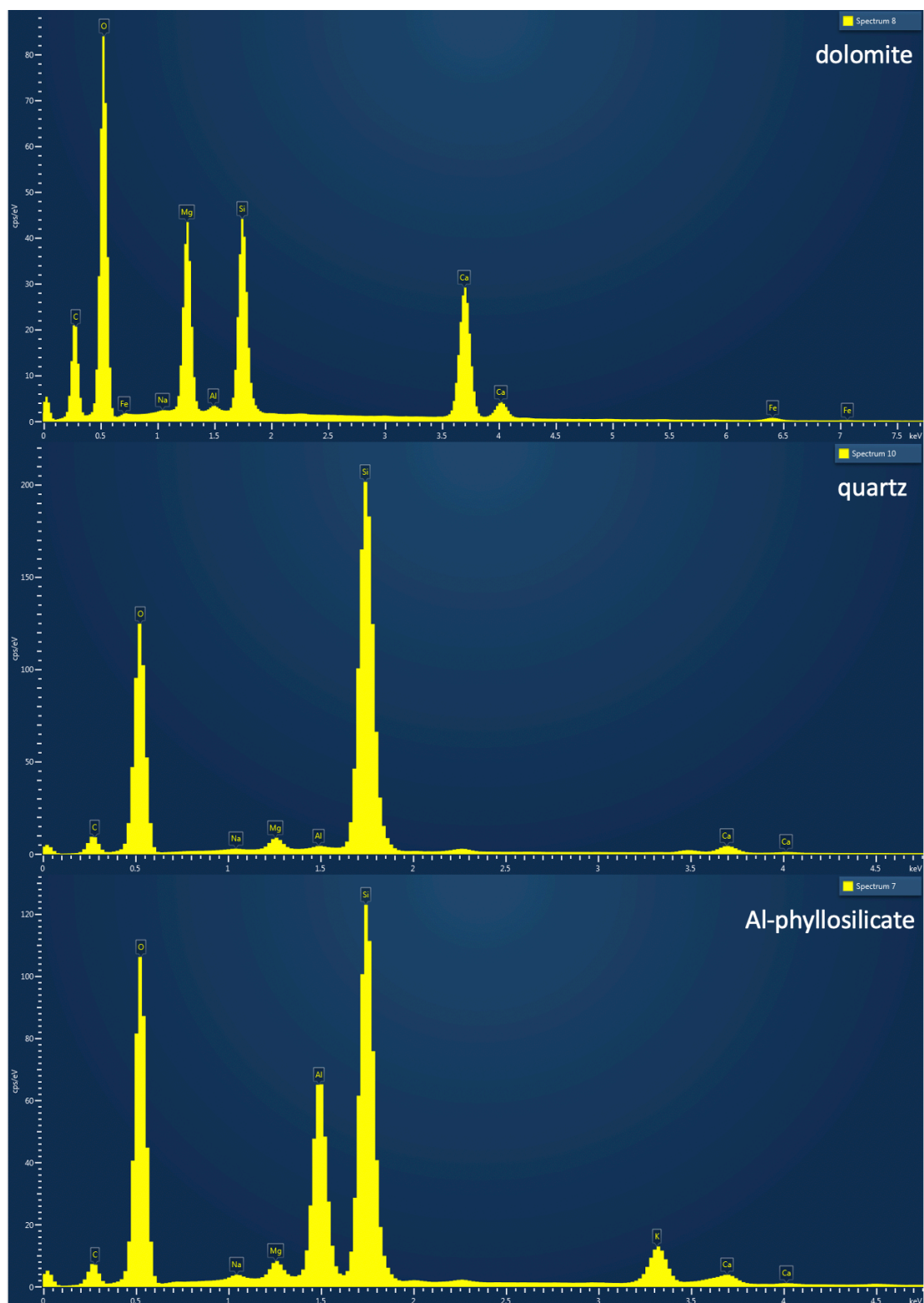
Figure S-10   Representative EDS point analyses of major phases in the Skillogalee Dolomite stromatolites: dolomite, quartz and aluminous phyllosilicate.
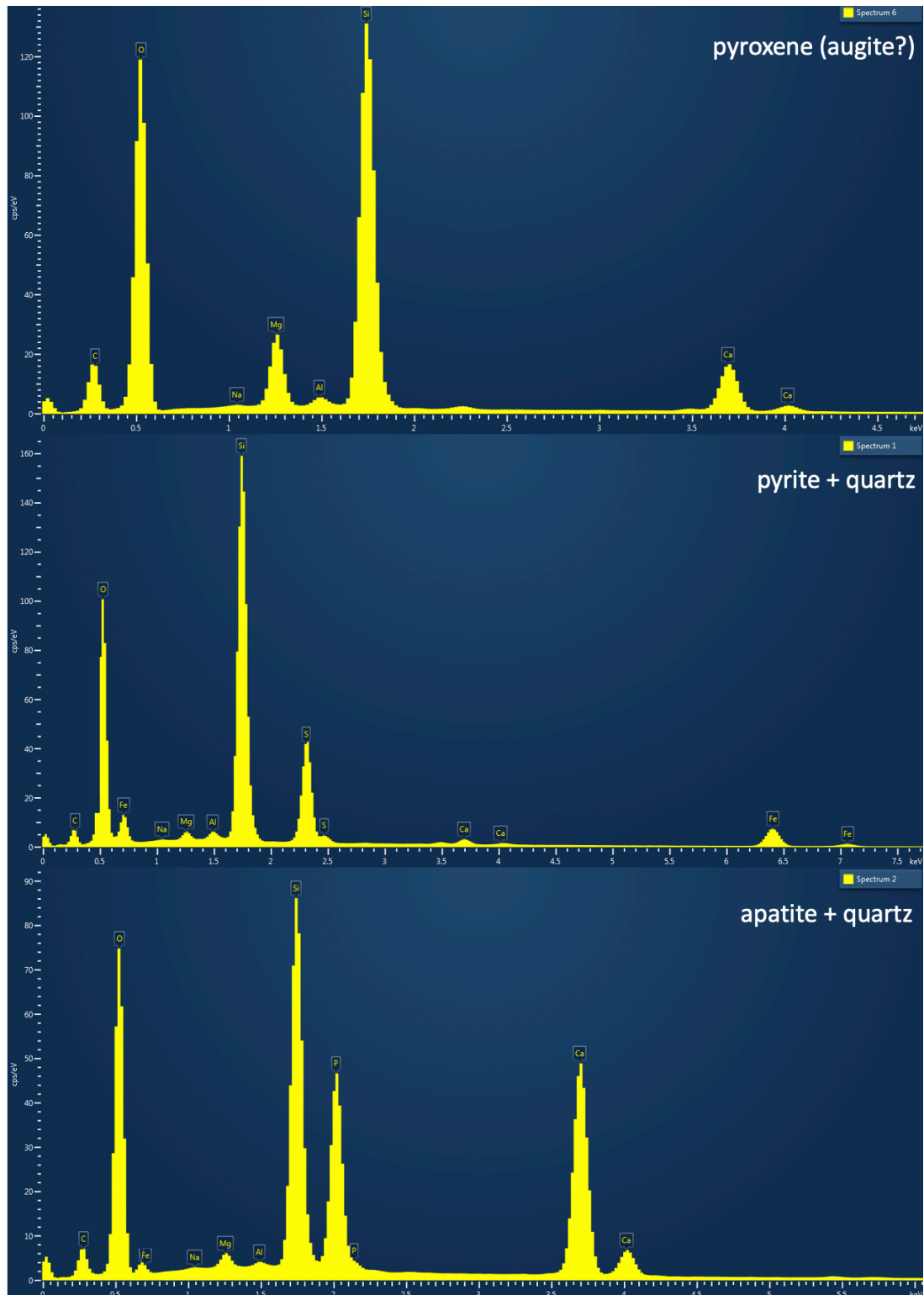
Figure S-11   Representative EDS point analyses of minor phases in the Skillogalee Dolomite stromatolites: pyroxene, pyrite and apatite. Pyrite and apatite occur as micrometric grains and thus the region of analysis features a large contribution from quartz.
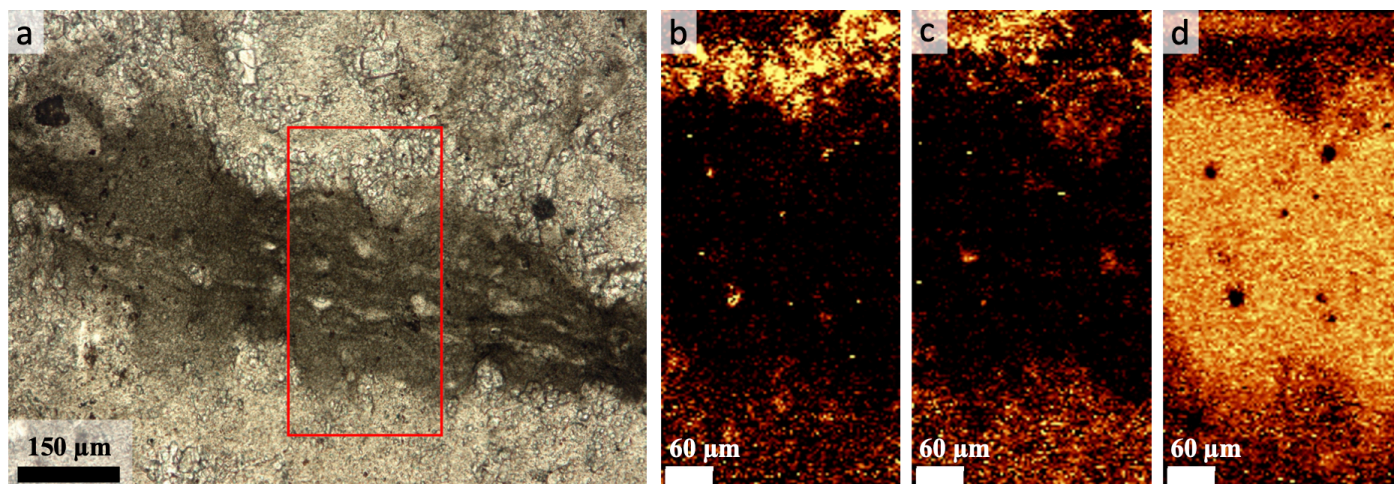
Figure S-12 Raman microspectroscopic mapping of Skillogalee Dolomite stromatolites. **(a)** Optical photomicrograph of organic material-rich layer; red box denotes region of **(b–d)**. **(b–d)** Raman mapping of dolomite, quartz and carbonaceous materials, respectively.
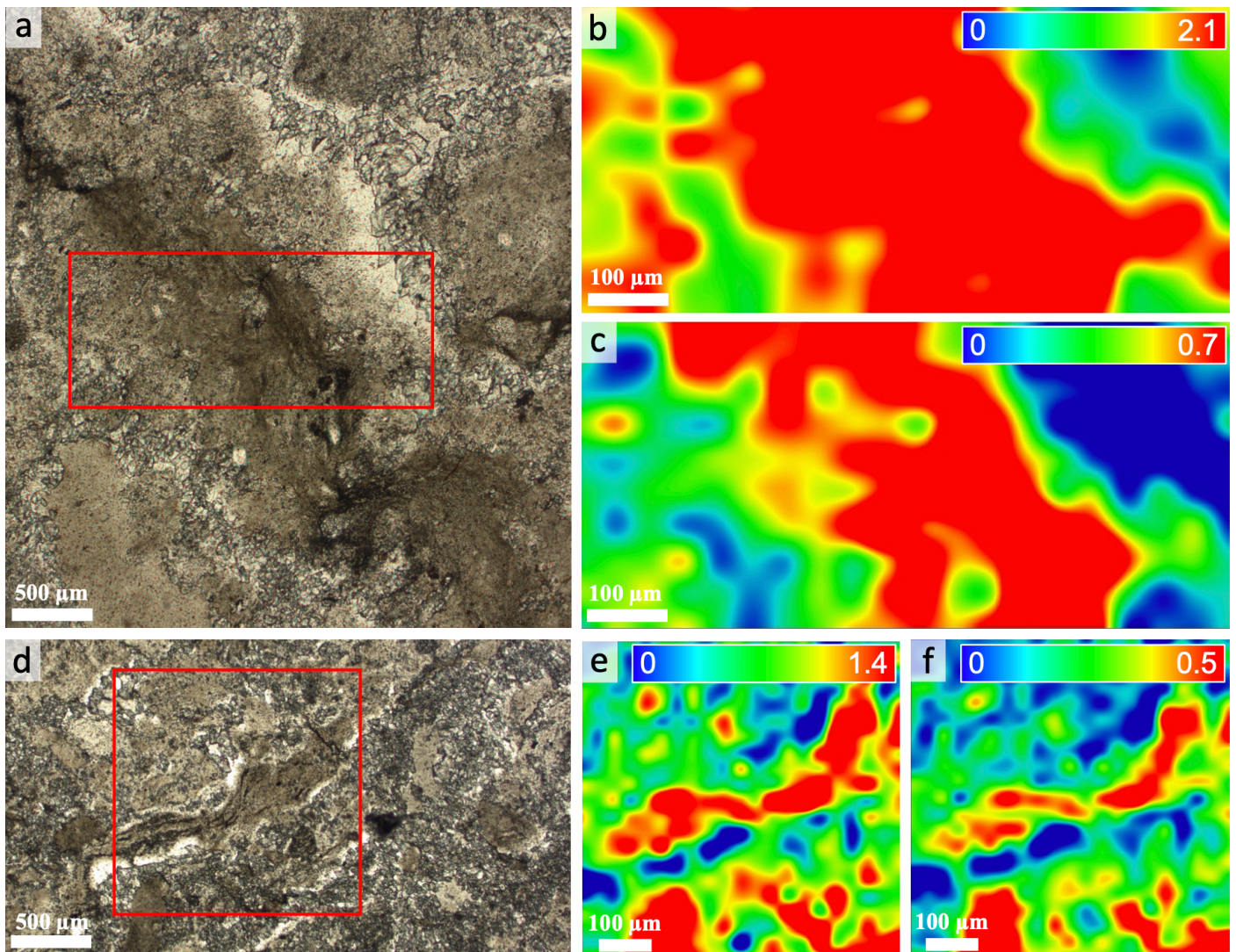
Figure S-13 FTIR microspectroscopic characterisation of organic materials in Skillogalee Dolomite stromatolites. **(a, d)** Optical photomicrographs and FTIR intensity maps of **(b, e)** the C=C band at 1600 cm^{-1} and **(c, f)** the C–H aliphatic band at 2850 cm^{-1}. FTIR maps correspond to red boxes in the optical photomicrographs. Colour scales given in absorbance units.
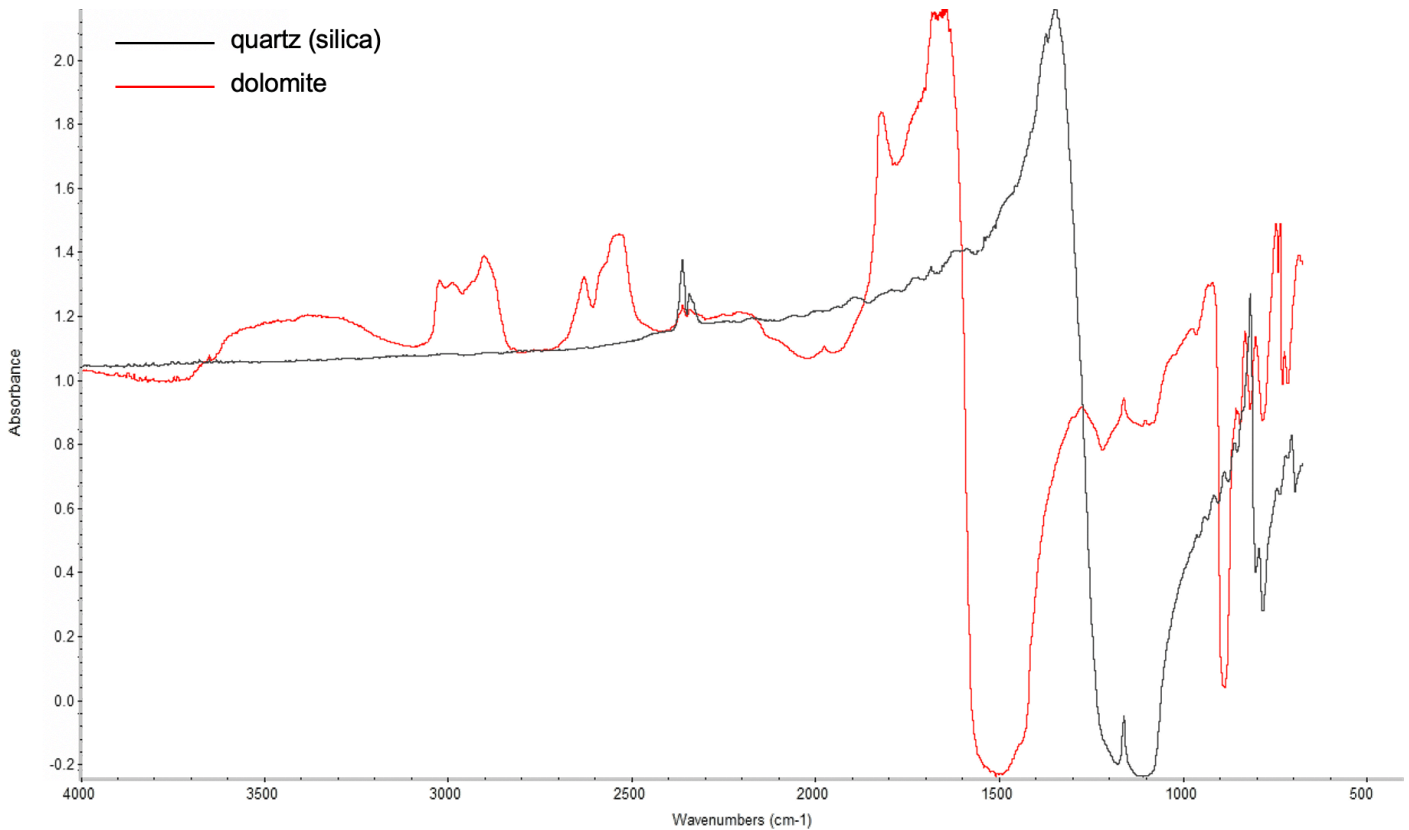
Figure S-14   Representative FTIR spectra acquired in the matrix of the Skillogalee Dolomite stromatolites. Spectra corresponding to both major phases of the matrix, *i.e.* microquartz (silica) and dolomite are shown. Note the absence or complete overprinting of the aliphatic C–H signatures in the 3000–2800 cm^{-1} region. Peaks corresponding to dolomite are as follows: 730, 2520, 2626, 2880, 2985 and 3020 cm^{-1}. Peaks corresponding to quartz are as follows: 793 and 1095 cm^{-1}. Features in both spectra between 2400 and 2100 cm^{-1} arise from atmospheric contributions.

Supplementary Information References

Beyssac, O., Goffé, B., Chopin, C., Rouzaud, J.N. (2002) Raman spectra of carbonaceous material in metasediments: a new geothermometer. *Journal of Metamorphic Geology* 20, 859–871. https://doi.org/10.1046/j.1525-1314.2002.00408.x

Fairchild, I.J., Kennedy, M.J. (2007) Neoproterozoic glaciation in the Earth System. *Journal of the Geological Society* 164, 895–921. https://doi.org/10.1144/0016-76492006-191

Fromhold, T.A., Wallace, M.W. (2012) Nature and significance of the Neoproterozoic Sturtian–Marinoan Boundary, Northern Adelaide Geosyncline, South Australia. *Australian Journal of Earth Sciences* 58, 599–613. https://doi.org/10.1080/08120099.2011.579624

Kouketsu, Y., Mizukami, T., Mori, H., Endo, S., Aoya, M., Hara, H., Nakamura, D., Wallis, S. (2014) A new approach to develop the Raman carbonaceous material geothermometer for low-grade metamorphism using peak width. *Island Arc* 23, 33–50. https://doi.org/10.1111/iar.12057

Preiss, W.V. (1971) *The biostratigraphy and palaeoecology of South Australian Precambrian stromatolites*. Ph.D. Thesis, University of Adelaide.

Preiss, W.V. (2000) The Adelaide Geosyncline of South Australia and its significance in Neoproterozoic continental reconstruction. *Precambrian Research* 100, 21–63. https://doi.org/10.1016/S0301-9268(99)00068-6

Preiss, W.V., Dyson, I.A., Reid, P.W., Cowley, W.M. (1998) Revision of lithostratigraphic classification of the Umberatana Group. *MESA Journal* 9, 36–42.

Virgo, G.M., Collins, A.S., Amos, K.J., Farkaš, J., Blades, M.L., Subarkah, D. (2021) Descending into the "snowball": High resolution sedimentological and geochemical analysis across the Tonian to Cryogenian boundary in South Australia. *Precambrian Research* 367, 106449. https://doi.org/10.1016/j.precamres.2021.106449